ACS APPLIED MATERIALS & INTERFACES

Research Article

www.acsami.org

One-Step Preparation of Graphene-Supported Anatase TiO_2 with Exposed {001} Facets and Mechanism of Enhanced Photocatalytic Properties

Liuan Gu, Jingyu Wang,* Hao Cheng, Yizhi Zhao, Lifei Liu, and Xijiang Han*

Department of Chemistry, Harbin Institute of Technology, Harbin 150001, China

Supporting Information

ABSTRACT: Anatase TiO_2 nanosheets supported on reduced graphene oxide (RGO) were synthesized via a one-step, solvothermal method. During the solvothermal step, graphene oxide (GO) was reduced to RGO, and, subsequently, anatase TiO_2 with 73.7% exposed {001} facets was grown in situ on the surfaces of the RGO nanosheets. Compared with pure TiO_2, the RGO/TiO_2 hybrid nanocomposite had improved photoactivity as a result of effective photoinduced electron transfer from TiO_2 to the RGO acceptor through interfacial interactions. Trapping tests showed that the oxidation of dye molecules proceeded for about 22% through the reaction with •OH radicals, and the remaining 78% occurred via direct interactions with holes. The holes left in TiO_2 crystals were the main reason for the enhanced photocatalytic properties of the RGO/TiO_2 composite. This paper not only reports the fabrication of highly active photocatalysts but also gives deeper insight into the photocatalytic mechanism of carbon/TiO_2 composites.

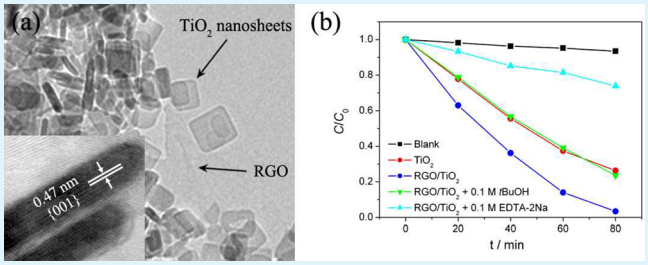

KEYWORDS: *RGO/TiO_2 hybrid nanocomposites, TiO_2 {001} facets, photocatalytic mechanism*

INTRODUCTION

Semiconductor photocatalysis has become a hot research area in recent decades because it is one of the most effective technologies for dealing with global environmental pollution and the energy crisis. Among various semiconductor photocatalysts, TiO_2-based materials have been the most promising candidates because of their strong oxidizing powers, photostabilities, and relative nontoxicities.[1−3] Carbon/TiO_2 composites have been reported as potential photocatalysts, and they can effectively enhance the charge-separation rate of TiO_2.[4−6] In comparison with traditional carbon materials, the honeycomb-like graphene has a very large π-conjugated system and a two-dimensional planar structure, and these improve the mobility of charge carriers (≈200000 cm^2 V^{-1} s^{-1}).[7−10] Graphene coupled with TiO_2, therefore, offers an effective way of accepting photoinduced electrons from the TiO_2 conduction band (CB) and lengthening the lifetimes of photoinduced charge carriers.[11−14] In addition, the highly transparent morphology, resulting from its one-atom thickness, will not significantly weaken the light intensity arriving at the catalyst surface. Since the first report of the synthesis of graphene/TiO_2 nanocomposites by Williams et al.,[15] these nanocomposites have been developed as efficient composite systems for applications in photocatalysis,[11,16,17] hydrogen production,[12] lithium-ion batteries,[18] and dye-sensitized solar cells.[19] For example, Liang et al. reported that a graphene/TiO_2 hybrid showed a 3-fold performance enhancement over that of commercial P25 in the degradation of rhodamine B.

Anatase TiO_2 nanosheets with reactive {001} facets exhibited photocatalytic activity superior to that of P25.[4,20−22] Both theoretical and experimental evidence show that the {001} facets are much more reactive than the thermodynamically stable {101} facets, as a result of their higher surface energy. Very recently, graphene-coupled TiO_2 with exposed {001} facets has been studied by several groups.[14,23−25] Sun et al. discovered that the introduction of graphene further improved the photocatalytic performance of TiO_2 as well as enhanced crystal facet engineering.[14] Some experiments, such as X-ray photoelectron spectroscopy (XPS) and X-ray absorption spectroscopy measurements, have been conducted to explain the interactions between TiO_2 and carbon materials, and they suggest that electron transfer is involved in the mechanism of enhanced photocatalysis.[5,25]

However, the contributions of active species, produced by photoinduced carriers on graphene and TiO_2, to the degradation of organics are still unclear because of a lack of sufficient evidence. The role of holes versus •OH radicals in the oxidation of organics remains controversial. For example, on naked TiO_2, the UV-assisted oxidation of phenol proceeds for 90% through reaction with surface-bound •OH radicals; the remaining 10% occurs via direct interactions with holes.[26] For polyaniline/TiO_2 nanocomposites, radicals were the main

Received: December 28, 2012
Accepted: March 25, 2013
Published: March 25, 2013

   dx.doi.org/10.1021/am303274t | ACS Appl. Mater. Interfaces 2013, 5, 3085−3093

active species that oxidized adsorbed organic pollutants under visible light, whereas holes were the main active species that functioned under UV light.[27] To the best of our knowledge, there is still no direct evidence for the mechanism of enhanced photocatalytic performance in graphene/TiO_2 composites.

In this paper, we present a one-step, solvothermal synthesis of graphene-supported anatase TiO_2 sheets with a high percentage of exposed {001} facets. More importantly, the detailed mechanism of enhanced photocatalytic properties as a result of graphene coupling is studied from several aspects. XPS and IR measurements showed the interfacial interactions between graphene and TiO_2, which facilitate electron transfer from TiO_2 to reduced graphene oxide (RGO). Photoluminescence spectra showed that the recombination rate of electrons and holes was lower in the composite system. The study of active species can explain the role of electron transfer between highly reactive TiO_2 and graphene in the reactivity properties of photocatalysts. Overall, this work provides a further understanding of the photocatalytic mechanism over carbon-supported TiO_2 nanomaterials and facilitates their applications in environmental purification and solar-energy conversion.

EXPERIMENTAL SECTION

Materials Preparation. *Preparation of Graphene Oxide (GO).* GO was synthesized using a modified Hummers' method.[28] Typically, natural graphite was reacted with concentrated H_2SO_4, $NaNO_3$, and $KMnO_4$. H_2O_2 was then added to the mixture after completion of the reaction. The product was then washed and centrifuged with dilute HCl and deionized water several times. Finally, the precipitate was dried in an oven.

Synthesis of a RGO/TiO_2 Hybrid. Anatase TiO_2 nanosheets with exposed {001} facets were incorporated with RGO through a simple one-step, solvothermal route. In a typical experimental process, 8 mg of GO was dissolved in 15 mL of isopropyl alcohol by sonication for 30 min, to obtain a solution of GO nanosheets. Then, 4 mL of tetrabutyl titanate (TBT) was added, and the mixture was sonicated for another 30 min to form a uniform solution. Next, 0.5 mL of fluoric acid (40 wt %) was dropped into the solution under continuous stirring. Finally, the mixed solution was placed in a 40-mL dried Teflon autoclave, and the vessel was sealed and heated at 180 °C for 12 h. After solvothermal treatment, the reaction system was cooled to room temperature and washed several times with absolute ethanol and deionized water. The sample was collected by vacuum drying at 60 °C for 24 h and then milled into an ultrafine powder. The initial mass ratio of GO to TBT was calculated to be 0.2%. By variation of the dosage of GO, a series of RGO-supported TiO_2 nanocomposites were synthesized. For comparison, anatase TiO_2 nanosheets were prepared using a similar solvothermal procedure without GO. In addition, RGO was also obtained in the absence of both TBT and fluoric acid via the above solvothermal method.

Characterization. Powder X-ray diffraction (XRD) patterns were obtained over the diffraction angle range (2θ) 5−80° using an XRD-6000 X-ray diffractometer with Cu Kα radiation as the X-ray source (Shimadzu, Japan). Scanning electron microscopy (SEM) images were obtained using an FEI Inspect microscope. Transmission electron microscopy (TEM) images were obtained using an FEI Tecnai G2 T20 S-Twin microscope with an accelerating voltage of 200 kV (FEI, USA). Atomic force microscopy (AFM) images were obtained using a Bioscope scanning probe microscope (Bruker, USA) on freshly cleaved mica in tapping mode. Raman spectra were recorded using a JY HR800 spectrometer (Jobin−Yvon, France) in the backscattering geometry with a 458-nm argon-ion laser as the excitation source. X-ray photoelectron spectroscopy (XPS) measurements were performed using a PHI5700 ESCA system (Physical Electronics) with an Mg Kα X-ray source. The binding energy shifts were corrected using the C 1s level at 284.6 eV as an internal standard, to compensate for the surface-charging effect during data analysis. The surface elemental stoichiometry was determined from the ratios of peak areas corrected with empirical sensitivity factors. Fourier transform infrared (FT-IR) spectra were recorded using a Nicolet Avatar 360 FT-IR spectrometric analyzer in the range 400−4000 cm^{-1}, with KBr pellets. Thermogravimetric analysis (TGA) was performed using a Mettler-Toledo TGA/SDTA851e instrument, at a heating rate of 10 °C min^{-1}, from room temperature to 950 °C under an air atmosphere. The surface areas of the samples were measured using the Brunauer−Emmett−Teller (BET) method on an ASAP 2020M instrument in liquid nitrogen (Micromeritics, USA). Photoluminescence (PL) spectra were obtained using a fluorescence spectrometer (LS 55, PerkinElmer, USA). The excitation wavelength was 320 nm, with a scanning speed of 600 nm min^{-1}. The widths of the excitation slit and emission slit were both 10 nm.

Photocatalytic Tests. The photocatalytic activities of the as-obtained samples were measured by degrading aqueous solutions of methylene blue (MB) under UV-light irradiation. The photocatalyst (10 mg) was suspended in 10 mL of an aqueous solution containing 40 μL of 0.2 wt % MB and HCl (pH 2.5). A high-pressure 100-W mercury lamp was used as the UV-light source. Before irradiation, the suspensions were stirred for about 40 min in the dark to establish an adsorption−desorption equilibrium. Self-decomposition of MB and the adsorption capacities of the photocatalysts for the dye molecules were both tested by determining the MB remaining after stirring in the dark. At given time intervals, the suspension was sampled for analysis by recording the MB absorption spectra. The changes in maximum absorption versus irradiation time (C/C_0 versus t) were obtained; these reflected the decrease in the MB concentration.

Detection of Reactive Oxygen Radicals ($^{\bullet}OH$ and $O_2^{\bullet-}$). A Bruker A200S spectrometer (Germany) was used to record the electron paramagnetic resonance (EPR) signals of radicals spin-trapped by 5,5-dimethyl-1-pyrroline *N*-oxide (DMPO) at ambient temperature. The parameters for the EPR measurements were as follows: center field, 3510 G; microwave frequency, 9.86 GHz; power, 2.28 mW.

To measure the level of $^{\bullet}OH$ radicals, 10 mg of photocatalyst was suspended in 50 mL of an aqueous solution containing 20 mM NaOH and 6 mM terephthalic acid (TA). The solution was stirred in the dark for 40 min before exposure to UV light. After illumination with a high-pressure 100-W mercury lamp for 20 min, the suspension was centrifuged, and the supernatant was sampled for analysis by recording the fluorescence signal of the generated 2-hydroxyterephthalic acid (TAOH) on a fluorescence spectrometer (LS 55, PerkinElmer, USA). The wavelength of the excitation light was 312 nm, and the scanning speed was 600 nm min^{-1}. The widths of the excitation slit and the emission slit were both 5 nm.

Trapping Tests for Radicals and Holes. The trapping experiments for photogenerated radicals and holes were carried out using *tert*-butanol (*t*-BuOH, radical scavenger) and ethylenediaminetetraacetic acid disodium salt (EDTA-2Na; hole scavenger). For the trapping of photogenerated radicals, a 0.1 M *t*-BuOH aqueous solution containing HCl (pH 2.5) was first prepared, and then 10 mg of photocatalyst was suspended in 10 mL of this aqueous solution. Subsequently, 40 μL of 0.2 wt % MB was added; the next step in the experimental process was the same as that in the above photocatalytic tests. For the hole-trapping experiments, the experimental procedure was similar to the radical one, except that EDTA-2Na was used instead of *t*-BuOH.

RESULTS AND DISCUSSION

The synthesis of the RGO/TiO_2 composite nanostructure is illustrated in Scheme 1. Briefly, GO prepared using a modified Hummers' method and TBT were mixed in an isopropyl alcohol solvent. After ultrasonic pretreatment, the strong van der Waals interactions among the layers of GO were overcome, leading to the generation of dispersed GO nanosheets. Meanwhile, TBT was dissolved and anchored on the GO surface via chemisorption with the oxygen-containing functional groups of GO at the molecular level.[29] In the following

Scheme 1. Schematic Illustration of Incorporating Anatase TiO_2 with Exposed {001} Facets into RGO to the Formation of RGO/TiO_2 Nanocomposites

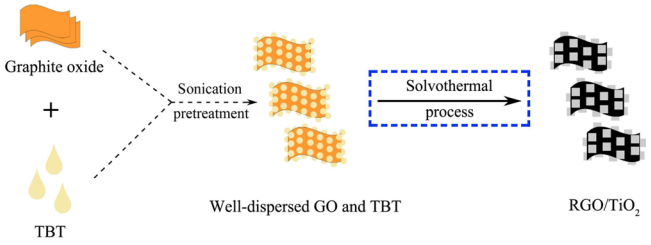

solvothermal procedure, GO was reduced to reduced GO (RGO) sheets, on which an anatase TiO_2 nanosheet with reactive {001} facets was in situ grown, thus forming composite RGO/TiO_2 nanostructures.

Structural Characterization. XRD was used to determine the crystallographic structures of as-prepared GO, RGO, TiO_2, and RGO/TiO_2 nanocomposites. As shown in Figure S1 in the Supporting Information (SI), only a strong diffraction peak at around 12.2° was observed, indicating the (002) diffraction of GO and the oxidation of natural graphite by expanding the *d* spacing from 0.35 to 0.52 nm.[30] After solvothermal treatment, this characteristic peak almost disappeared and a weak diffraction peak from RGO appeared at 23.0°, suggesting that most of the GO was reduced.[6] According to the standard pattern (JCPDS 21-1272), the pure TiO_2 nanosheets and RGO/TiO_2 nanocomposites both existed in the pure anatase phase (Figure 1). Notably, no typical RGO diffraction peaks

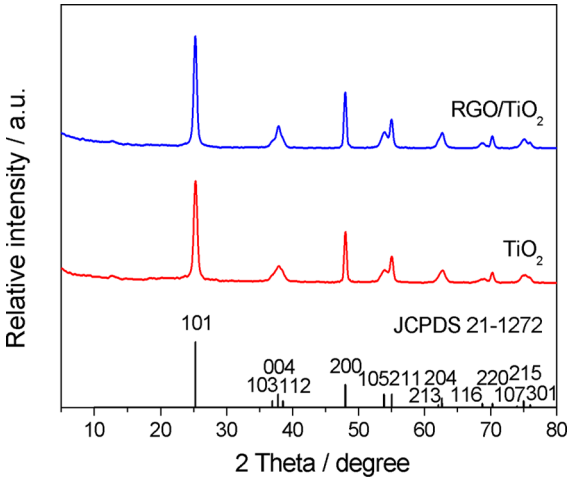

Figure 1. XRD patterns of as-obtained TiO_2 and RGO/TiO_2.

were observed in the RGO/TiO_2 pattern because the weak RGO diffraction peak at 23.0° was shielded by the stronger peak of TiO_2 at 25.3°.[31]

TEM and high-resolution TEM (HRTEM) images clearly demonstrated the morphology and structure of the as-synthesized samples (Figure 2). As shown in Figure 2a,b and as reported in the literature, the free-standing, two-dimensional GO sheets were not flat but crumpled, with a layered structure.[12,25] As a result of surface-terminated oxygen-containing functional groups such as −OH and −COOH, the obtained GO could be well dispersed in polar solvents to form homogeneous solutions (inset in Figure 2b). Parts c and d of Figure 2 show that sheetlike anatase TiO_2 nanocrystals of average length 32.5 nm and thickness 5.8 nm were grown in situ on the RGO layers. The HRTEM image further confirmed the morphology and crystal characteristics of the anatase TiO_2 crystals in the RGO/TiO_2 composite nanostructure (Figure 2e). The typical laterally viewed hexagonal shape in Figure 2e was observed through the [100] zone axis, which was consistent with our previous work.[22] The lattice spacing was found to be 0.47 nm, corresponding to the reactive {001} facets of anatase TiO_2. The reactive {001} facets were calculated to account for about 73.7% of TiO_2 in the RGO/TiO_2 composite, using a geometric calculation. For comparison, images of a pure TiO_2 sample are given as Figure 2f and an inset. The percentage of {001} facets in pure TiO_2, with an average length of 33.8 nm and a thickness of 5.9 nm, was calculated to be ca. 74.1%, which differed slightly from the parameters in the composite. In the absence of RGO, the dispersion of the TiO_2 crystals was much poorer, although RGO has little influence on the crystal phase of TiO_2. As a result, the RGO layers could serve as a supporting material for in situ growth of anatase TiO_2 nanocrystals and suppressed aggregation.[25] This kind of interfacial interaction would facilitate the transfer of photoinduced electrons from TiO_2 to RGO when using the composite for photocatalysis.

Dilute suspensions of GO and the RGO/TiO_2 hybrid were dropped onto freshly cleaved mica and then analyzed using AFM; the results are shown in Figure 3. The cross-sectional analysis showed a height of about 3 nm for the GO sheet (Figure 3a,b). It is well-known that the thickness of graphene is increased by the introduction of bulky carbonyl, epoxy, and carboxyl groups on the surface when graphene is oxidized to GO.[32] Gomez-Navarro et al. and Stankovich et al. reported that the thickness of a single GO sheet was typically 0.9−1.3 nm, determined by AFM, indicating that the GO obtained in our case might be a trilayer sheet.[33,34] For the hybrid in Figure 3c, it was obvious that the RGO sheet was coupled to TiO_2 nanoparticles. However, the RGO in the hybrid was even thicker (4.3 nm) than the GO sheet (3.2 nm; Figure 3c,d), which was probably the result of stacking of single RGO layers during the reduction process.

Raman spectroscopy, a powerful nondestructive tool, was used to confirm the successful oxidation of natural graphite using the modified Hummers' method and the combination with TiO_2. As shown in Figure 4, the graphite displayed two distinct Raman response signals, i.e., a D band at 1366 cm^{-1} and a G band at 1578 cm^{-1}. The D peak, from sp^3 hybridization, indicated disruption of the symmetrical hexagonal graphitic lattice by internal structural defects, edge defects, and dangling bonds, whereas the G peak, indicating sp^2 hybridization, originated from the in-plane stretching motion of symmetric C−C bonds. The D and G bands of GO differed from those of graphite in three aspects: (i) a significant increase in the D/G intensity ratio (I_D/I_G) from 0.11 to 0.76, which arose from disruption of the lattice symmetry; (ii) broadening of both the D and G peaks as a result of the introduction of hydroxyl and epoxy groups; (iii) shifts of the D band from 1366 to 1372 cm^{-1} and the G band from 1578 to 1592 cm^{-1}, as a result of the increased numbers of isolated carbon double bonds in disordered GO.[35] The results demonstrated that natural graphite had been largely oxidized by the modified Hummers' method. For the RGO/TiO_2 composite, D and G bands could also be observed in the range 1200−1800 cm^{-1}. As in the case of the presence of oxygen-containing functional groups in GO, the introduction of TiO_2 led to shifts of the D and G bands, as well as an increase in I_D/I_G (from 0.11 to 0.73)

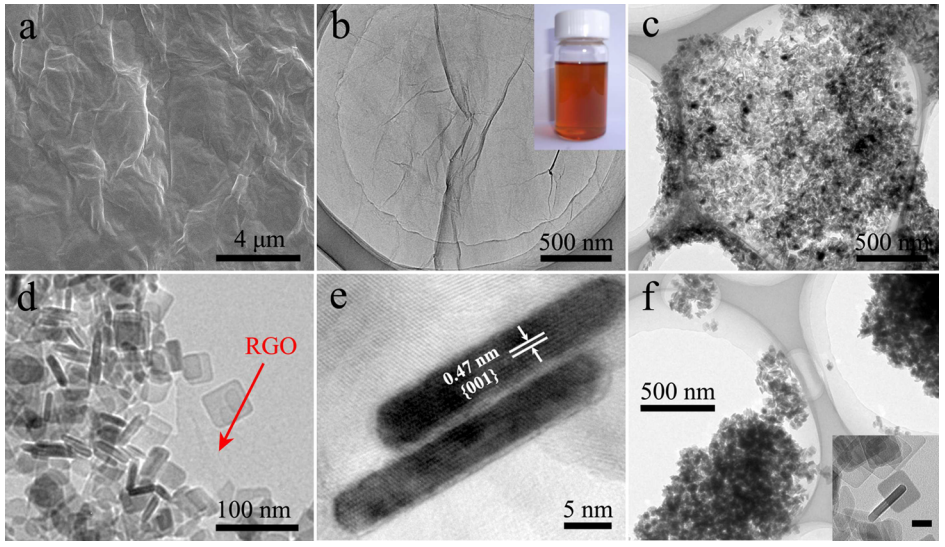

Figure 2. Representative SEM, TEM, and HRTEM images of GO and RGO/TiO_2: (a) SEM image of GO; (b) TEM image of GO (inset is the solution of GO dispersed in isopropyl alcohol); (c) low-magnification TEM image of RGO/TiO_2; (d) high-magnification TEM image of RGO/TiO_2; (e) HRTEM image of anatase TiO_2 nanosheets in RGO/TiO_2; (f) low-magnification TEM image of the obtained anatase TiO_2 sample (inset is the high-magnification TEM image; scale bar 20 nm).

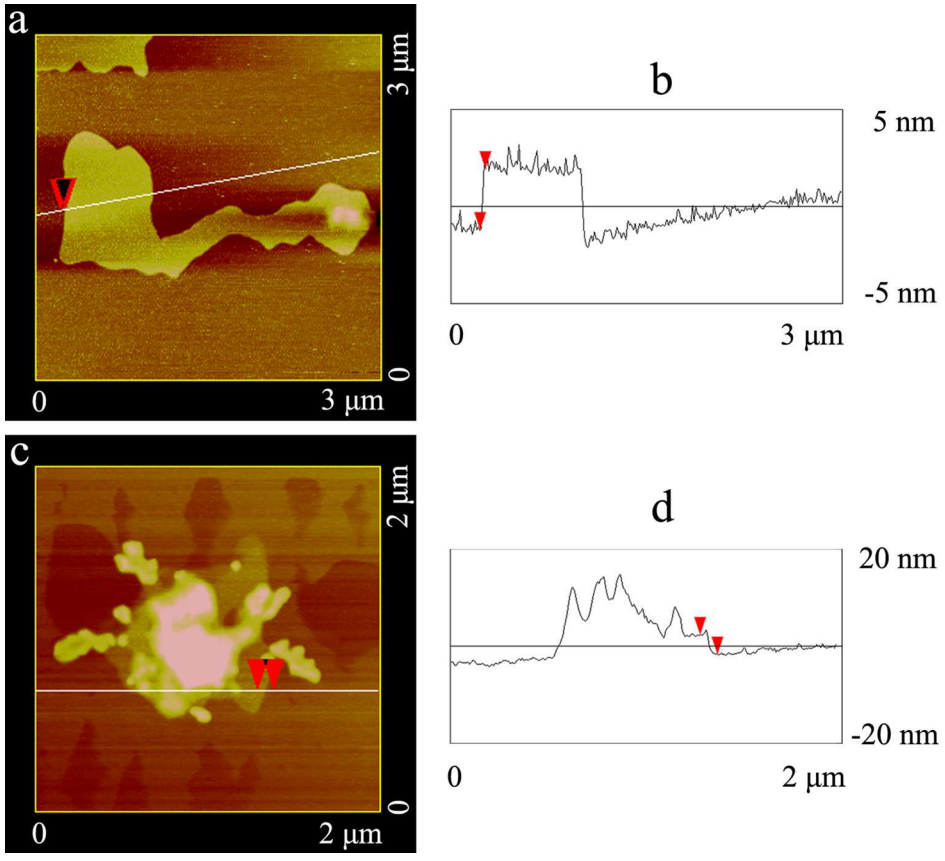

Figure 3. (a) AFM image of GO. (b) Depth profile of the line of interest on the GO sheet (the red marker corresponds to the GO sheet with a height of 3.2 nm). (c) AFM image of the RGO/TiO_2 hybrid. (d) Depth profile of the line of interest on RGO/TiO_2 (the red marker corresponds to the RGO sheet in the hybrid with a height of 4.3 nm).

in the RGO/TiO_2 composite. These shifts of the D and G bands in RGO/TiO_2 were deduced to be the result of interfacial interactions with TiO_2.

During the solvothermal process, the color of the reaction solution changed from brown to black, indicating that GO was reduced to RGO under high temperature and pressure. The evolution of oxidized carbon species was studied by XPS (Figure 5). The C 1s core-level spectrum of GO could be devolved into four peaks at 284.5, 286.7, 287.9, and 289.0 eV, corresponding to elemental carbon, C−O in hydroxyl or epoxy

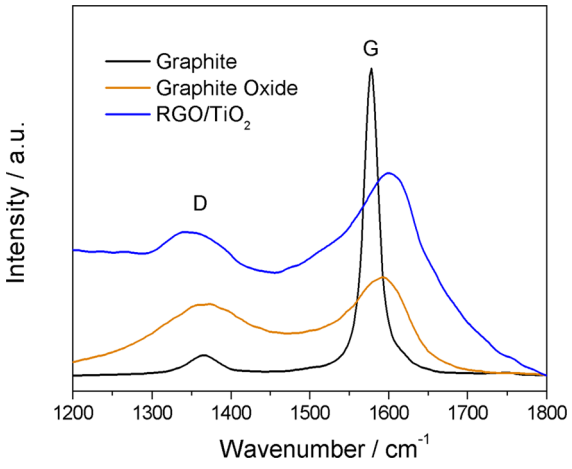

Figure 4. Raman spectra of natural graphite and graphite oxide.

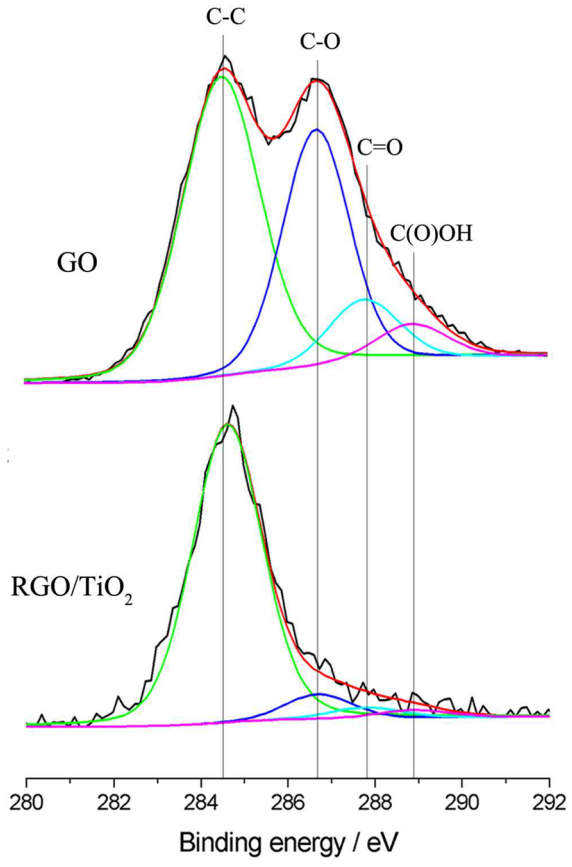

Figure 5. High-resolution XPS spectra of C 1s for GO and RGO/TiO_2.

groups, C═O, and C(O)O, respectively.[36,37] After the solvothermal reaction, all of the peaks from oxygen-containing functional groups weakened sharply, suggesting substantial removal of hydroxyl, epoxy, carbonyl, and carboxyl groups.[14] The reduction degree of GO was calculated to be 75.6% from the changes in the peak areas of the carbon species in GO and RGO/TiO_2 (48.0% of oxidized carbon for GO and 11.7% of that for RGO/TiO_2). Compared with photoassisted synthesis, the solvothermal method was more efficient at removing oxygen-containing functional groups in GO.[35,38] It should be noted that no peak was detected at around 281 eV, implying that elemental carbon had not been doped into the TiO_2 lattice.[39] The RGO−TiO_2 interactions in the composite were also investigated using XPS. As shown in Figure 6, two peaks

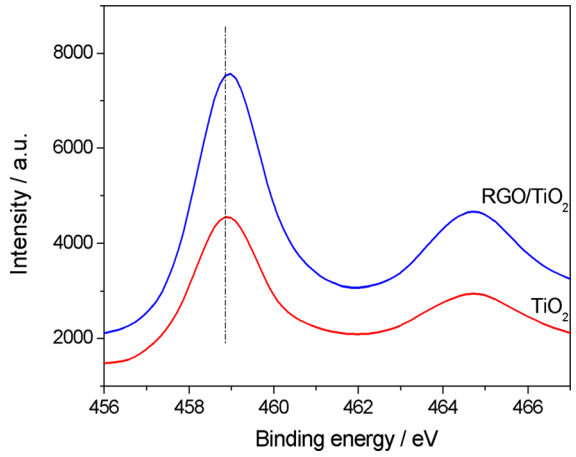

Figure 6. XPS spectra of Ti 2p over GO and RGO/TiO_2.

from pure TiO_2 were observed at 458.85 and 464.73 eV, which were respectively assigned to the Ti $2p_{3/2}$ and Ti $2p_{1/2}$ spin−orbital splitting photoelectrons in the Ti^{4+} chemical states. After the introduction of RGO, the Ti $2p_{3/2}$ peak shifted slightly toward higher binding energy, to 458.98 eV. This shift of 0.13 eV could be explained by a change in the chemical state or coordination environment of Ti $2p_{3/2}$,[5,40] i.e., the interactions between RGO and TiO_2.

The reduction of GO was also confirmed using FT-IR measurements (Figure 7). The peaks of GO at 1053, 1281,

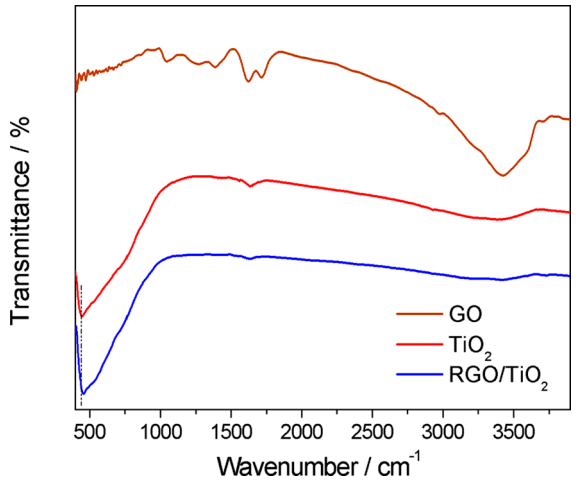

Figure 7. FT-IR spectra of GO and the RGO/TiO_2 nanocomposite.

1396, 1726, and 3433 cm^{-1} were assigned to oxygen-containing functional groups, i.e., C−O (alkoxy) stretching, C−OH stretching, O−H deformation, C═O stretching, and O−H stretching, respectively. In the spectrum of RGO/TiO_2, these characteristic absorption bands decreased dramatically in intensity or even disappeared entirely, indicating a significant reduction of GO by solvothermal treatment. The peak at 1633 cm^{-1} was assigned to the skeletal vibrations of unoxidized graphitic domains.[41] The strong absorption band centered at 457 cm^{-1} was attributed to the Ti−O−Ti stretching vibrations in TiO_2-based composites.[42] The slight blue shift compared with the absorption band of the Ti−O−Ti stretching vibration

dx.doi.org/10.1021/am303274t | ACS Appl. Mater. Interfaces 2013, 5, 3085−3093

in pure TiO_2 (centered at 447 cm^{-1}) indicated interfacial interactions between RGO and TiO_2 in the composite. In addition, TGA was used to confirm the real content of RGO in the RGO/TiO_2 composite. Upon heating, a total weight loss of about 5.9% was observed below 950 °C, including 1.2% from adsorbed water vapor between room temperature and 100 °C and 4.7% from the combustion of RGO in the RGO/TiO_2 composite above 100 °C in air (Figure S2 in the SI).

Evaluation of the Photocatalytic Efficiency. The influence of RGO coupling on the photocatalytic activity of TiO_2 was studied through MB degradation. It is noteworthy that there were no significant changes in the BET specific areas of the photocatalysts (79.0 m^2 g^{-1} for pure TiO_2 and 76.8 m^2 g^{-1} for the RGO/TiO_2 composite; Figure S3 in the SI). The enhanced adsorptivity of RGO/TiO_2, as seen in Figure S4 in the SI, therefore did not merely originate from simple physical adsorption but was largely the result of selective adsorption of the aromatic dye on the catalyst. The adsorption was noncovalent and driven by $\pi-\pi$ stacking between MB and the aromatic regions of the graphene.

As shown in Figure 8, the activity of the RGO/TiO_2 composite photocatalyst was higher than that of a reference

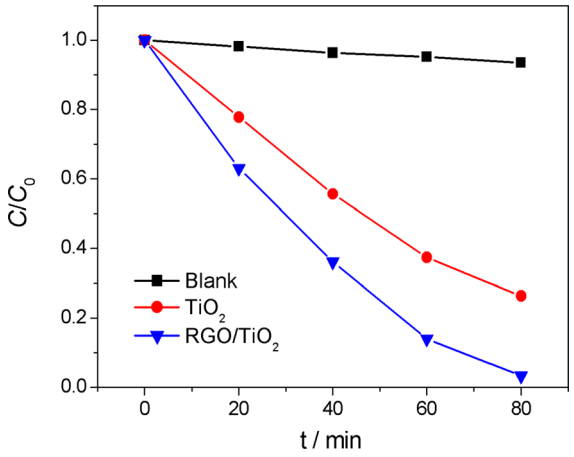

Figure 8. Photocatalytic activities of TiO_2 and RGO/TiO_2 as a function of time for degradation of MB under UV-light illumination.

sample of TiO_2 under UV-light illumination. Graphene has been reported to be a competitive acceptor material because of its two-dimensional π-conjugated structure.[43] The two-dimensional planar structure endows it with unexpectedly good conductivity and benefits the transport of charge carriers.[44] On the basis of these two factors, photoexcited electrons could rapidly transfer from the CB of TiO_2 to RGO through interfacial interactions. The recombination of electron−hole (e^-−h^+) pairs could therefore be greatly suppressed in the composite system, leaving more charge carriers to react with water, dissolved O_2, and dye molecules.

In addition, the amount of incorporated GO has some effect on the photoactivity of the composite.[17] All of the RGO/TiO_2 composites exhibited a better photocatalytic performance than did pure TiO_2, as seen in Figure S5 in the SI. However, excess RGO shielded some of the light arriving at TiO_2, which lowered the quantum efficiency of the photocatalyst. Also, a large covering of RGO might occupy active sites on the TiO_2 surface and block subsequent reactions with water, dissolved O_2, and dye molecules.

Mechanism of Enhancement of the Photocatalytic Properties in the RGO/TiO_2 System. In general, photocatalytic processes involve the excitation, bulk diffusion, and surface transfer of photoinduced charge carriers. As mentioned above, the function of RGO in the TiO_2 photocatalytic system was mainly focused on charge transport between their contacting surfaces. The separated carriers participated in MB degradation, and most of the photogenerated e^-−h^+ pairs inevitably recombined at the surface or at bulk trapping sites, with the release of photons and heat, resulting in PL. To clarify the function of RGO in the TiO_2 photocatalytic system, PL was used to study the excited state and reveal the differences in the photocatalytic efficiencies of the photocatalysts because PL emission arises from the recombination of free carriers.[45,46] PL spectra of the RGO/TiO_2 composite and pure TiO_2 in the wavelength range 350−550 nm are shown in Figure 9.

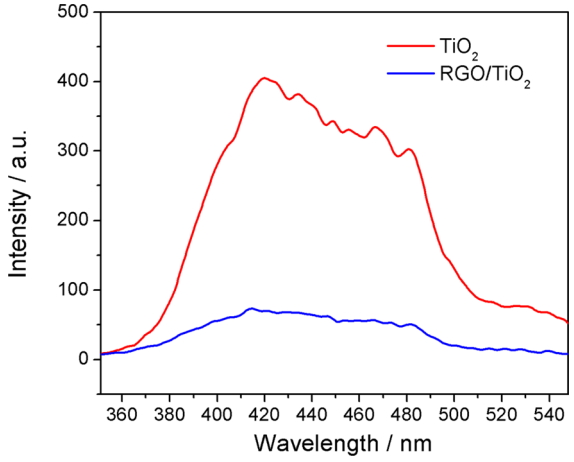

Figure 9. PL spectra of as-prepared TiO_2 and RGO/TiO_2 solid powders.

Obviously, the TiO_2 sample emitted strong PL signals with peaks at 420, 434, 449, 467, and 481 nm. The introduction of RGO led to a significant decrease in the emission intensity of the PL spectrum, compared with that of pure TiO_2, indicating a much lower recombination rate of photoinduced electrons and holes. The PL results demonstrated that the RGO layers with a two-dimensional π-conjugated structure could serve as an effective electron-accepting material and hinder the direct recombination of e^-−h^+ pairs in TiO_2.

In order to obtain more information about the mechanism of MB photodegradation, EPR measurements were used to detect the intermediate radicals (mainly $^{\bullet}OH$ and $O_2^{\bullet-}/HO_2^{\bullet}$) generated in the RGO/$TiO_2$ photocatalytic system under UV light. Because it was very hard to detect $^{\bullet}OH$ and $O_2^{\bullet-}/HO_2^{\bullet}$ directly under steady-state EPR measurements, because of their high reactivities and short lifetimes, DMPO is often used as $^{\bullet}OH$ or $O_2^{\bullet-}/HO_2^{\bullet}$ traps to form relatively stable species.[47,48] Figure 10a shows the EPR spectrum of the hybrid in water under UV light; the spectrum displays the characteristic 1:2:2:1 signal of the DMPO−$^{\bullet}OH$ adduct.[47] This result indicated the presence of $^{\bullet}OH$ during the photocatalytic process over the hybrid under UV light.

Because the lifetime of DMPO−$O_2^{\bullet-}/HO_2^{\bullet}$ was much shorter than that of DMPO−$^{\bullet}OH$ in water, the hybrid was dispersed in ethanol to detect $O_2^{\bullet-}/HO_2^{\bullet}$.[49] As shown in Figure 10b, the EPR pattern had the signature of the DMPO−

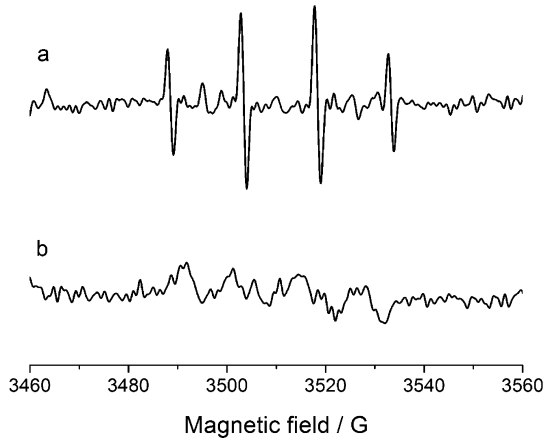

Figure 10. DMPO spin-trapping EPR spectra over the RGO/TiO_2 hybrid under UV light for (a) a hydroxyl radical ($^{\bullet}OH$) in water and (b) a superoxide radical ($O_2^{\bullet-}$) in ethanol.

$O_2^{\bullet-}/HO_2^{\bullet}$ adduct, but it seemed to be much weaker in intensity than that of the DMPO−$^{\bullet}OH$ adduct.

To further illustrate the relationship between the carrier separation and photocatalytic properties in the RGO/TiO_2 composite, a TA fluorescence probe was used to monitor the level of $^{\bullet}OH$ radicals generated in the reaction system under UV-light irradiation. TA reacts with $^{\bullet}OH$ to form TAOH, so the fluorescence intensity of TAOH was related to the level of $^{\bullet}OH$ radicals produced in the photocatalytic system. As a result of a lower degree of recombination and the longer lifetimes of the carriers in the composite system, the fluorescence signal of TAOH was stronger than that of TiO_2, indicating that more valid e^-−h^+ pairs participated in the radical-chain reaction and more $^{\bullet}OH$ groups were generated (Figure 11).

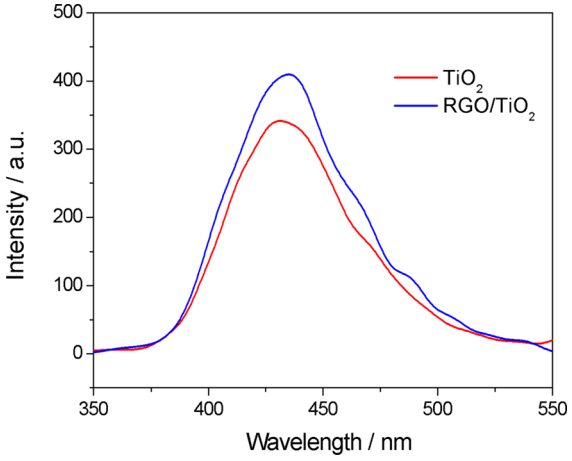

Figure 11. Fluorescence signal intensity of TAOH over TiO_2 and RGO/TiO_2 after UV-light irradiation.

From the above analysis of electron transfer between RGO and TiO_2, the photocatalytic processes in the RGO/TiO_2 composite system were proposed to involve generation, separation, transfer of e^-−h^+ pairs, and a chain reaction. Under UV-light irradiation, TiO_2 particles directly absorb photons, exciting electrons from the valence band (VB) to the CB. The generated e^-−h^+ pairs are unstable and tend to recombine quickly, leading to a serious decrease in the quantum efficiency and impairment of the photoactivity.[50] However, in the presence of RGO, with a π-conjugated structure, these photoinduced electrons can transfer from the CB of TiO_2 to the RGO surface and then react with oxygen to yield reactive oxygen species such as $O_2^{\bullet-}$, $HO_2^{\bullet}$, and $^{\bullet}OH$.[23,44] The main oxidative species, holes left in the VB of TiO_2, will transfer to the surface and directly oxidize the adsorbed dye molecules, as well as reacting with water to produce $^{\bullet}OH$ radicals.

In this case, the recombination of photogenerated electrons and holes is suppressed, and their lifetime is prolonged. RGO-hybridized TiO_2 exhibited enhanced photocatalytic efficiency for the degradation of organic pollutants. However, the mechanism of the enhancement of the photocatalytic properties of RGO/TiO_2 is still unclear because of the lack of evidence regarding the roles of holes versus $^{\bullet}OH$ radicals in the degradation of organics. To clarify the contributions of holes and $^{\bullet}OH$ radicals, *t*-BuOH (a radical scavenger) and EDTA-2Na (a hole scavenger) were used as probes to detect the main oxidative species in the photocatalytic process of RGO/TiO_2 under UV light. The results of the trapping experiments, shown in Figure 12, showed that the addition of the radical scavenger

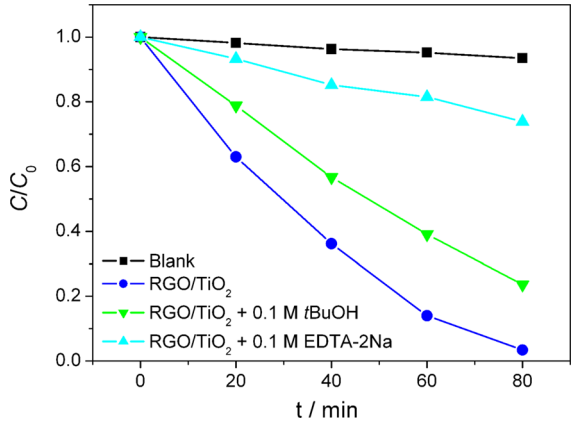

Figure 12. Trapping test of photogenerated holes and hydroxyl radicals in the RGO/TiO_2 composite system.

(*t*-BuOH) only caused a small decrease in the photoactivity of the RGO/TiO_2 composite. However, when the hole scavenger (EDTA-2Na) was added to the photocatalytic system, the photocatalytic activity was seriously suppressed. The oxidation of MB dye proceeded for about 22% through reactions with $^{\bullet}OH$ radicals, and the remaining 78% occurred via direct interactions with holes. The major reactions occurring in this system are summarized in Scheme 2. These results revealed that photoinduced holes were the main oxidative species in the RGO/TiO_2 photocatalytic systems under UV light.[27] Through the effective separation of carriers, the enhancement of the photocatalytic performance by RGO introduction mainly comes from holes left in TiO_2 crystals rather than electrons transferring to RGO.

CONCLUSIONS

In summary, RGO/TiO_2 hybrid nanocomposites were synthesized using a one-step, solvothermal method, with GO and TBT as the starting materials. Through the introduction of RGO sheets as a two-dimensional substrate, anatase TiO_2 nanocrystals with a large percentage of exposed {001} facets were grown in situ on the RGO surface, with a uniform distribution. During the solvothermal process, the efficient

Scheme 2. Proposed Mechanism of the RGO/TiO_2 Composite Material during a UV Photocatalytic Process

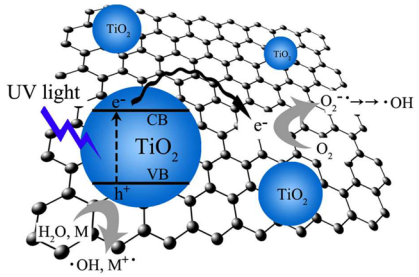

$RGO/TiO_2 + h\nu \rightarrow RGO/TiO_2(e^-\text{-}h^+)$

$RGO/TiO_2(e^-\text{-}h^+) \rightarrow RGO(e^-)/TiO_2(h^+)$

$e^- + O_2 \rightarrow O_2^{-\cdot}$ (→ → $HO_2^{\cdot}$, H_2O_2, ·OH)

$h^+ + H_2O \rightarrow H^+ + \cdot OH$

ROS + M → $M^{+\cdot}$ --- 22%

$h^+ + M \rightarrow M^{+\cdot}$ --- 78%

$M^{+\cdot}$ → → oxidation products

removal of oxygen-containing functional groups in GO (reduction degree of 75.6%) and the combination with highly reactive TiO_2 were achieved. XPS and IR analyses suggested that interfacial interactions occurred between RGO and TiO_2. The EPR results confirmed the existence of abundant $^{\bullet}OH$ radicals and a small number of $O_2^{\bullet-}$ radicals in the photocatalytic reaction. PL measurements and $^{\bullet}OH$ radical tests showed that RGO could serve as an effective electron-accepting material, resulting in the effective separation of photogenerated e^-–h^+ pairs. The lower recombination rate and longer lifetimes of electrons and holes brought about the enhanced photocatalytic activity of the composite system. Through trapping experiments, it was further shown that the enhancement mainly came from holes left in the TiO_2 crystals rather than electrons transferring to RGO. Confirmation of the exact influence of RGO incorporation would be useful for an in-depth study of the photocatalytic mechanism in carbon/TiO_2 composites and for the development of photocatalysts with high activities.

■ ASSOCIATED CONTENT

Supporting Information

XRD patterns of GO and RGO, TGA curve of a RGO/TiO_2 composite, nitrogen adsorption–desorption isotherms and corresponding pore-size distributions of RGO/TiO_2 and TiO_2 samples, adsorptivity of TiO_2 and RGO/TiO_2 hybrid to dye molecules, and the effect of the mass ratio of GO to TBT on the photocatalytic activities over RGO/TiO_2 nanocomposites. This material is available free of charge via the Internet at http://pubs.acs.org.

■ AUTHOR INFORMATION

Corresponding Author

*Tel.: 86-451-86413702. Fax: 86-451-86418750. E-mail: jingyu.wang@163.com (J.W.), hanxj63@yahoo.com.cn (X.H.).

Notes

The authors declare no competing financial interest.

■ ACKNOWLEDGMENTS

This work was supported by the National Natural Science Foundation of China (Grants 21001037, 21071037, and 91122002), the Specialized Research Fund for the Doctoral Program of Higher Education of China (Grant 20092302120073), and the Fundamental Research Funds for the Central Universities (Grant HIT.NSRIF.2009058).

■ REFERENCES

(1) Chen, X. B.; Mao, S. S. *Chem. Rev.* **2007**, *107*, 2891–2959.
(2) Kongkanand, A.; Tvrdy, K.; Takechi, K.; Kuno, M.; Kamat, P. V. *J. Am. Chem. Soc.* **2008**, *130*, 4007–4015.
(3) Pan, X.; Zhao, Y.; Liu, S.; Korzeniewski, C. L.; Wang, S.; Fan, Z. Y. *ACS Appl. Mater. Interfaces* **2012**, *4*, 3944–3950.
(4) Chen, J. S.; Liu, H.; Qiao, S. Z.; Lou, X. W. *J. Mater. Chem.* **2011**, *21*, 5687–5692.
(5) Zhang, H. B.; Pan, X. L.; Liu, J. Y.; Qian, W. Z.; Wei, F.; Huang, Y. Y.; Bao, X. H. *ChemSusChem* **2011**, *4*, 975–980.
(6) Zhu, P. N.; Nair, A. S.; Peng, S. J.; Yang, S. Y.; Ramakrishna, S. *ACS Appl. Mater. Interfaces* **2012**, *4*, 581–585.
(7) Geim, A. K.; Novoselov, K. S. *Nat. Mater.* **2007**, *6*, 183–191.
(8) Allen, M. J.; Tung, V. C.; Kaner, R. B. *Chem. Rev.* **2010**, *110*, 132–145.
(9) Banhart, F.; Kotakoski, J.; Krasheninnikov, A. V. *ACS Nano* **2011**, *5*, 26–41.
(10) Mattevi, C.; Kim, H.; Chhowalla, M. *J. Mater. Chem.* **2011**, *21*, 3324–3334.
(11) Du, J.; Lai, X. Y.; Yang, N. L.; Zhai, J.; Kisailus, D.; Su, F. B.; Wang, D.; Jiang, L. *ACS Nano* **2011**, *5*, 590–596.
(12) Zhang, X. Y.; Li, H. P.; Cui, X. L.; Lin, Y. H. *J. Mater. Chem.* **2010**, *20*, 2801–2806.
(13) Li, N.; Liu, G.; Zhen, C.; Li, F.; Zhang, L. L.; Cheng, H. M. *Adv. Funct. Mater.* **2011**, *21*, 1717–1722.
(14) Sun, L.; Zhao, Z. L.; Zhou, Y. C.; Liu, L. *Nanoscale* **2012**, *4*, 613–620.
(15) Williams, G.; Seger, B.; Kamat, P. V. *ACS Nano* **2008**, *2*, 1487–1491.
(16) Liu, J. C.; Bai, H. W.; Wang, Y. J.; Liu, Z. Y.; Zhang, X. W.; Sun, D. D. *Adv. Funct. Mater.* **2010**, *20*, 4175–4181.
(17) Jiang, B. J.; Tian, C. G.; Zhou, W.; Wang, J. Q.; Xie, Y.; Pan, Q. J.; Ren, Z. Y.; Dong, Y. Z.; Fu, D.; Han, J. L.; Fu, H. G. *Chem.—Eur. J.* **2011**, *17*, 8379–8387.
(18) Qiu, Y. C.; Yan, K. Y.; Yang, S. H.; Jin, L. M.; Deng, H.; Li, W. S. *ACS Nano* **2010**, *4*, 6515–6526.
(19) Sun, S. R.; Gao, L.; Liu, Y. Q. *Appl. Phys. Lett.* **2010**, *96*, 083113.
(20) Yang, H. G.; Sun, C. H.; Qiao, S. Z.; Zou, J.; Liu, G.; Smith, S. C.; Cheng, H. M.; Lu, G. Q. *Nature* **2008**, *453*, 638–641.
(21) Han, X. G.; Kuang, Q.; Jin, M. S.; Xie, Z. X.; Zheng, L. S. *J. Am. Chem. Soc.* **2009**, *131*, 3152–3153.
(22) Gu, L. A.; Wang, J. Y.; Cheng, H.; Du, Y. C.; Han, X. J. *Chem. Commun.* **2012**, *48*, 6978–6980.
(23) Xiang, Q. J.; Yu, J. G.; Jaroniec, M. *Nanoscale* **2011**, *3*, 3670–3678.
(24) Ding, S. J.; Chen, J. S.; Luan, D. Y.; Boey, F. Y. C.; Madhavibc, S.; Lou, X. W. *Chem. Commun.* **2011**, *47*, 5780–5782.
(25) Jiang, B. J.; Tian, C. J.; Pan, Q. J.; Jiang, Z.; Wang, J. Q.; Yan, W. S.; Fu, H. G. *J. Phys. Chem. C* **2011**, *115*, 23718–23725.
(26) Minero, C.; Mariella, G.; Maurino, V.; Vione, D.; Pelizzetti, E. *Langmuir* **2000**, *16*, 8964–8972.
(27) Zhang, H.; Zong, R. L.; Zhao, J. C.; Zhu, Y. F. *Environ. Sci. Technol.* **2008**, *42*, 3803–3807.
(28) Cote, L. J.; Kim, F.; Huang, J. *J. Am. Chem. Soc.* **2009**, *131*, 1043–1049.
(29) Tang, Y. B.; Lee, C. S.; Xu, J.; Liu, Z. T.; Chen, Z. H.; He, Z. B.; Cao, Y. L.; Yuan, G. D.; Song, H. S.; Chen, L. M.; Luo, L. B.; Cheng, H. M.; Zhang, W. J.; Bello, I.; Lee, S. T. *ACS Nano* **2010**, *4*, 3482–3488.

(30) Kovtyukhova, N. I.; Ollivier, P. J.; Martin, B. R.; Mallouk, T. E.; Chizhik, S. A.; Buzaneva, E. V.; Gorchinskiy, A. D. *Chem. Mater.* **1999**, *11*, 771−778.
(31) Xu, Y. J.; Zhuang, Y. B.; Fu, X. Z. *J. Phys. Chem. C* **2010**, *114*, 2669−2676.
(32) Schniepp, H. C.; Li, J. L.; McAllister, M. J.; Sai, H.; Herrera-Alonso, M.; Adamson, D. H.; Prud'homme, R. K.; Car, R.; Saville, D. A.; Aksay, I. A. *J. Phys. Chem. B* **2006**, *110*, 8535−8539.
(33) Gomez-Navarro, C.; Weitz, R. T.; Bittner, A. M.; Scolary, M.; Mews, A.; Burghard, M.; Kern, K. *Nano Lett.* **2007**, *7*, 3499−3503.
(34) Stankovich, S.; Dikin, D. A.; Piner, R. D.; Kohlhaas, K. A.; Kleinhammes, A.; Jia, Y.; Wu, Y.; Nguyen, S. T.; Ruoff, R. S. *Carbon* **2007**, *45*, 1558−1565.
(35) Bell, N. J.; Ng, Y. H.; Du, A. J.; Coster, H.; Smith, S. C.; Amal, R. *J. Phys. Chem. C* **2011**, *115*, 6004−6009.
(36) Stankovich, S.; Piner, R. D.; Chen, X. Q.; Wu, N. Q.; Nguyen, S. T.; Ruoff, R. S. *J. Mater. Chem.* **2006**, *16*, 155−158.
(37) Mattevi, C.; Eda, G.; Agnoli, S.; Miller, S.; Mkhoyan, K. A.; Celik, O.; Mastrogiovanni, D.; Granozzi, G.; Garfunkel, E.; Chhowalla, M. *Adv. Funct. Mater.* **2009**, *19*, 2577−2583.
(38) Lambert, T. N.; Chavez, C. A.; Bell, N. S.; Washburn, C. M.; Wheeler, D. R.; Brumbach, M. T. *Nanoscale* **2011**, *3*, 188−191.
(39) Yang, X. X.; Cao, C. D.; Ericson, L.; Hohn, K.; Maghirang, R.; Klabunde, K. *J. Catal.* **2008**, *260*, 128−133.
(40) Li, J.; Tang, S. B.; Lu, L.; Zeng, H. C. *J. Am. Chem. Soc.* **2007**, *129*, 9401−9409.
(41) Nethravathi, C.; Rajamathi, M. *Carbon* **2008**, *46*, 1994−1998.
(42) Tang, F.; Hou, L.; Guo, G. *J. Inorg. Mater.* **2001**, *16*, 615−619.
(43) Liu, Q.; Liu, Z. F.; Zhang, X. Y.; Yang, L. Y.; Zhang, N.; Pan, G. L.; Yin, S. G.; Chen, Y. S.; Wei, J. *Adv. Funct. Mater.* **2009**, *19*, 894−904.
(44) Zhang, H.; Lv, X. J.; Li, Y. M.; Wang, Y.; Li, J. H. *ACS Nano* **2010**, *4*, 380−386.
(45) Yu, J. C.; Yu, J. G.; Ho, W. K.; Jiang, Z. T.; Zhang, L. Z. *Chem. Mater.* **2002**, *14*, 3808−3816.
(46) Zhang, W. F.; Zhang, M. S.; Yin, Z.; Chen, Q. *Appl. Phys. B* **2000**, *70*, 261−265.
(47) Kochany, J.; Bolton, J. R. *J. Phys. Chem.* **1991**, *95*, 5116−5120.
(48) Hidaka, H.; Zhao, J.; Pelizzetti, E.; Serpone, N. *J. Phys. Chem.* **1992**, *96*, 2226−2230.
(49) Kochany, J.; Bolton, J. R. *J. Phys. Chem.* **1991**, *95*, 5116−5120.
(50) Yu, J. G.; Wang, W. G.; Cheng, B.; Su, B. L. *J. Phys. Chem. C* **2009**, *113*, 6743−6750.